Acta Geotechnica (2009) 4:233–247
DOI 10.1007/s11440-009-0093-4

RESEARCH PAPER

# Analyses on granular mass movement mechanics and deformation with distinct element numerical modeling: implications for large-scale rock and debris avalanches

**Nick Thompson · Matthew R. Bennett · Nick Petford**

Received: 2 February 2009 / Accepted: 6 May 2009 / Published online: 7 July 2009


**Abstract** A large-scale avalanche of Earth material is modeled here as a granular flow using a distinct element numerical model $PFC^{2D}$. Such failures occur in a variety of geological settings and are known to occur frequently over geologic time-scales transporting significant volumes of material basinward. Despite this, they remain poorly understood. The model used here begins with a listric failure, typical of the flank collapse of a volcanic cone, and describes the movement of an assembly of several thousand particles from failure to deposition. Within the model, each particle possesses its own material properties and interacts with its immediate neighbors and/or the basal boundary during emplacement. The general mechanics of the particle assembly are observed by monitoring the stresses, displacements, and velocities of distinct sections of the avalanche body. We monitor the avalanches' energy regime (e.g., gravitational influence, energy dissipation by friction, kinetic energy evolution, and avalanche body strain). The addition of colored markers of varying geometry to the pre-failure avalanche was also used to make qualitative observations on the internal deformation that occurs during avalanche emplacement. A general stretching and thinning of the avalanche is observed. Monitoring of vertical and horizontal variations in stress, strain, porosity, and relative particle stability indicate that the lower more proximal sections of the avalanche are subject to higher stresses. These stresses are observed to be most significant during the initial phases of failure but decline thereafter; a situation likely to be conducive to block fragmentation and in developing a basal shear layer in real-world events. The model also shows how an avalanche which is initially influenced purely by gravity (potential energy) develops into a fully flowing assemblage as downslope momentum is gained and kinetic energy increases. The horizontal transition where the failure meets the run-out surface is recognized as a key area in emplacement evolution. The model has particular relevance to volcanic flank collapses and consequently the implications of the model to these types of failure and the geological products that result are considered in detail although the model is relevant to any form of large-scale rock or debris avalanche.

**Keywords** Avalanche emplacement · Distinct element modeling · Fragmentation · Landslide mechanics · Rock avalanches · Volcanic debris avalanches

## 1 Introduction

The rapid downslope movement of Earth material in response to gravity is an important mass movement process and is commonly believed to behave as a granular flow [4, 5, 13, 27, 34, 35, 49]. These events range from small-scale slope failures to much larger rock and debris avalanches, for example, volcanic edifice collapses that may involve volumes in excess of $10^6$ $m^3$ [24]. Large-scale failures of this type remain poorly understood due to their inaccessibility to conventional field survey and therefore alternative methods such as numerical modeling are commonly employed for analysis [5, 6, 42, 49, 50]. Distinct element modeling (DEM) is one widely adopted approach to this type of problem which models the motion and interaction of rigid, typically circular or spherical, particles within a granular assembly. The advantage of using DEM in

N. Thompson (✉) · M. R. Bennett · N. Petford
Bournemouth University, Poole, UK
e-mail: nthompson@bournemouth.ac.uk

analyzing avalanche motion in comparison to continuum-based techniques is that individual particles within an avalanche can be assigned specific material properties and the interaction and separation of these particles *within* the failure can be monitored. Consequently, emerging spatial variations in assembly properties can be examined within the moving avalanche, thereby allowing the controlling processes to be explored during avalanche emplacement. Earlier studies [6, 8–10] have established DEM as an appropriate tool for modeling the flow of granular materials.

The aim of this paper is to use DEM to explore the emplacement of large granular avalanches associated with the collapse of volcanic edifices, such as that which occurred at on the 18 May, 1980 at Mount St. Helens, USA, in 1980. Such methods have been previously applied to the stability and failure of volcanic edifices [28–31, 44, 45, 50]. In contrast to these studies, the focus here is on the processes and deformations that occur through a vertical slice of the avalanche (2D) after the initiation of failure initiation as opposed to pre-failure evolution or deposit distribution.

A commercially available DEM software package, $PFC^{2D}$, was chosen for this study and configured to give an unbonded assembly of granular particles. The code is based on the work of Cundall [11] and Cundall and Strack [12] and simulates the dynamic relationship of a group of moving, rigid particles by calculating the contact forces and subsequent displacements of each individual particle in response to its interaction with its neighbors [22]. Calculations are performed over sufficiently small timesteps such that disturbances cannot transmit further than the immediate neighbors of a particular particle [22]. Continuous, explicit solving of the dynamic equations of motion allows for realistic modeling of flowing particle assemblies [26]. Movements of stressed assemblies continue until forces in a given simulation are balanced or completely dissipated by friction and/or one of the available forms of system damping [22].

Similar approaches have been used previously to investigate granular avalanche emplacement, both to simulate laboratory-type experiments [6, 10, 40] and reproduce real-world avalanches [2, 10, 17, 32, 42]. A wealth of topics have been investigated in these studies including the spatial variation in particle velocities with time during emplacement, runout dependence on failure volume, and primary influences on final deposit geometry. This article builds upon these investigations, however, using an initial geometry that is designed specifically to replicate a volcanic edifice flank failure rather than a more generic slope failure. In addition, a more detailed study of the mechanical processes occurring during emplacement and deformation of the granular avalanche is undertaken using software tools and analysis methods previously not available or considered in earlier studies. Specifically, the stress histories, relative displacement, and velocity of each section of the avalanche mass are examined throughout emplacement. Vertical and horizontal variations in assembly properties, such as strain rate and porosity, are then considered. The chosen software also allows a range of energy histories to be examined, enabling the driving and deposition mechanisms of granular avalanche movement and deformation to be recorded. Finally, using various colored markers, it is possible to assess qualitatively the deformation of the failure mass over a range of different material properties and configurations.

## 2 Model setup

An initial failure model based on a typical volcanic edifice flank collapse (e.g., [21, 38, 46]) was designed (Fig. 1). The use of a pre-defined failure surface is favored for several reasons: (1) the study is concerned only with the processes that occur *after* flank failure and failure mechanisms are not considered; (2) little is known about the location of major discontinuities within volcanic edifices [33]; and (3) using additional particles to create a complete cone significantly increases computing time and prohibitively increases run time. The edifice model shown in Fig. 1 has a maximum height of 1,000 m and a slope angle of 30°, a flank angle typical of large stratovolcanoes [36]. The failure space is created by defining a surface which rises at an initial angle of 7° to the horizontal following the models of Voight and Elsworth [47] and Voight [46]. The runout surface is horizontal.

Particles, treated as disks of unit thickness, are filled into the failure space and subjected to gravity until they reach equilibrium although they remain restrained by the retaining flank wall as depicted in Fig. 1. Although a certain degree of stress builds up in the toe of the failure due to this procedure, it does not significantly affect the emplacement process as long as the particles remain unbounded. The final pre-failure model consists of 16,578

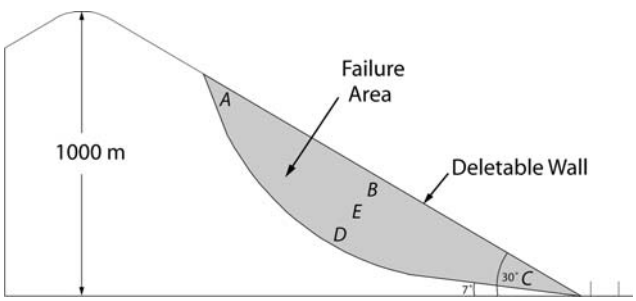


**Fig. 1** Pre-failure simulation edifice. Letters *A*–*E* depict the locations of particles included in the mechanical analysis as described in Sect. 3

particles with a uniform size distribution ranging in size from 3.2 to 5.3 m in diameter (particle size ratio of 1.66). No specific assumptions are made as to the initial material properties of the particles in the model, and consequently assumptions are avoided with respect to the nature of the rock mass involved. The pre-failure avalanche mass is simply a particulate assembly at a certain initial geometry where each particle is in contact with its immediate neighbors and/or the failure surface. Gravity is the only force to which the assembly is subject. As a result size-scaling procedures are not necessary. The size range and distribution for the particles used in the model represent a balance between model resolution and practical simulation processing time since it is virtually impossible to represent accurately the particle number and size distribution likely to be present in a real-world failure. Avalanche behavior at particles size ranges other than that specified was not investigated. Due to their circular shape and frictional coupling effects, particles inevitably roll during emplacement, both in relation to each other and the runout surface. As a result, a small number of particles separate from the distal extent of the avalanche mass after deposition of the main avalanche body, particularly at higher values of particle and wall friction. These few particles were not included in any displacement, velocity, or energy evaluations; runout distances are measured from the original location of the slope toe to the distal extent of the main avalanche body. Particle rolling was not restricted here for two reasons: (1) consistency with previous studies which have used DEM [5, 10] or laboratory methods [18] to investigate avalanche emplacement where particle rotation was not controlled, and; (2) block rolling, to some degree, occurs in real-world rock and debris avalanches and it is therefore unsuitable to ignore fully this motion and consider emplacement exclusively as block sliding. Several earlier studies have investigated slope mechanics using restricted particle rotation [28–31, 42]. In most of these studies, however, the static gravitational deformation of large-scale slope flanks was being examined rather than dynamic downslope avalanche motion. In the case of Tomassi [42], downslope motion was considered although only through frictional block sliding. As it seems inappropriate to completely inhibit particle rotation, a more realistic model for real-world avalanche behavior may entail a closer investigation of the effects of rolling and the dependency of this motion on material frictional properties. With the above limitations in mind, simulation results presented here should only be regarded as first-order approximations of real-world events.

The model properties are presented in Table 1 and were retained throughout all simulations. Particle normal/shear stiffness influences the computational timestep used; as this parameter was seen to have a negligible effect on avalanche behavior in earlier sensitivity analyses, common values used by Itasca [22] were employed. Wall normal/shear stiffness values were set equal to particle stiffness values for model stability. Particle density represents a common value for competent rock material. A viscous damping technique was used within PFC$^{2D}$ to ensure that the model reaches a reasonable equilibrium and is most appropriate for dynamic conditions in that numerical energy damping is enforced only at the instant of particle–particle contact and free-motion is not damped [22]. The chosen value corresponds to a restitution coefficient appropriate for that of competent rock material, approximately 0.7, and was obtained through simulation drop tests [1, 22]. Local damping, which applies a damping force to each ball proportional to the unbalanced force of the assembly, was not employed. Energy is also dissipated through friction when particles develop long-lasting contacts with each other or the basal runout surface using a linear contact model [22].

**Table 1** Particle and wall properties used for avalanche simulations; these parameters remained constant throughout the analysis

| Parameter | Value |
|---|---|
| Particle normal/shear stiffness (N/m) | 1E8 |
| Wall normal/shear stiffness (N/m) | 1E8 |
| Particle density (kg/m$^3$) | 2,000.0 |
| Viscous damping coefficient | 1.0 |

After the pre-failure slope has been sufficiently filled with particles and cycled to equilibrium under gravity to ensure a steady-state condition where each particle is in contact with its neighbors and the assembly would not settle further, the flank wall is deleted to induce failure. The avalanche begins to travel as the model is cycled and is monitored until movement ceases.

A sensitivity analysis was conducted to observe the effects of various initial wall ($\mu_w$) and particle ($\mu_p$) friction coefficients on the characteristics of the final avalanche deposit, namely, runout, displacement of the proximal section, maximum thickness, and the horizontal location of the section of maximum thickness. Similar back-analysis approaches have been used in previous numerical avalanche simulations (e.g., [23]). This analysis showed that $\mu_p$ had little effect on the final characteristics of the deposit, while the influence of $\mu_w$ was significant in affecting avalanche runout, which decreased significantly with increasing $\mu_w$. For instance, runout decreased from approximately 8 km with $\mu_w = 0.05$ to <1.5 km with $\mu_w = 0.3$. Consequently, the results presented in this article are based on findings from simulations conducted at a single combination of $\mu_w = 0.1$ for $\phi = 5.7°$ and

$\mu_p = 0.75$ for $\phi = 37°$, where $\phi = \tan^{-1}\mu$, except where specified otherwise. These values are chosen as they represent median values of those tested and produce a deposit with similar empirical relationships to those observed for large-scale volcanic debris avalanches ($H/L \sim 0.12$ per Ui [43]). In order to observe the influence of uninhibited particle rolling, a simulation was conducted at this combination of material friction values where particle rotation was completely restricted. The resultant particulate deposit was significantly different to that produced when rolling was not restricted as runout decreased, resulting in a thicker, shorter deposit ($H/L = 0.19$). However, as the deposit could not settle into a compact arrangement due to frictional coupling between adjacent particles, an unrealistic packing arrangement was observed. It is therefore confirmed that complete particle rolling restriction may be inappropriate and an approach whereby rolling is dependent on particle friction or material stiffness may be the best approach for future studies.

## 3 Mechanical analysis

In order to observe the geomechanical behavior of the travelling avalanche, a suite of variables was monitored throughout emplacement (Table 2). Each of these variables was monitored for a single particle located at five locations within the failure mass (A–E in Fig. 1). The particular locations represent the head, toe, and top, middle, and bottom of the medial section of the avalanche and were chosen as their range of responses represents the full range of avalanche behavior in terms of confinement, overburden, and influence of the ground and free surfaces. Only one particle from each section was used as a proxy for the whole section. To support this approach, identical mechanical variables were measured from several additional particles in each section. For instance, Fig. 2 shows the *x*-velocity and *xx*-stress component variables previously described but measured from two other particles in close proximity to particles A, B, C, D, and E. Plots for the other variables mentioned in Table 2 show similar results. Although some variation is observed, results are generally consistent and therefore it is reasonable to assume that the effects experienced by one particle in a certain section of the avalanche can be used as a good approximation for the general behavior of remainder of that section. The highest variability is seen in the stresses experienced by each particle as these values are originally highly erratic. Relative stress differences are generally preserved, however.

The horizontal displacement of the monitored particles increases rapidly then slows to a steady rate before declining rapidly immediately before movement ceases. The high initial rate of displacement reflects the chaotic moments just after failure where the avalanche begins to travel downslope. The unrestrained particle at the toe of the failure (C) travels the greatest distance, approximately 10 km, the particle at the head of the failure (A) the least distance, 1 km, and those located in the medial section (B, D, E) travel comparable distances, approximately 2 km.

**Table 2** Variables monitored for mechanical analysis of the travelling avalanche

| Variable | Description |
|---|---|
| Stress (*xx*-component) | Time-dependent stress in the *xx*-direction (MPa) |
| Stress (*xy*-component) | Time-dependent stress in the *xy*-direction (MPa) |
| Stress (*yy*-component) | Time-dependent stress in the *yy*-direction (MPa) |
| *x*-displacement | Total horizontal distance traveled by particle (m) |
| *x*-velocity | Time-dependent *x*-velocity (dimensionless) |
| *y*-displacement | Total vertical distance traveled by particle (m) |
| *y*-velocity | Time-dependent *y*-velocity (dimensionless) |

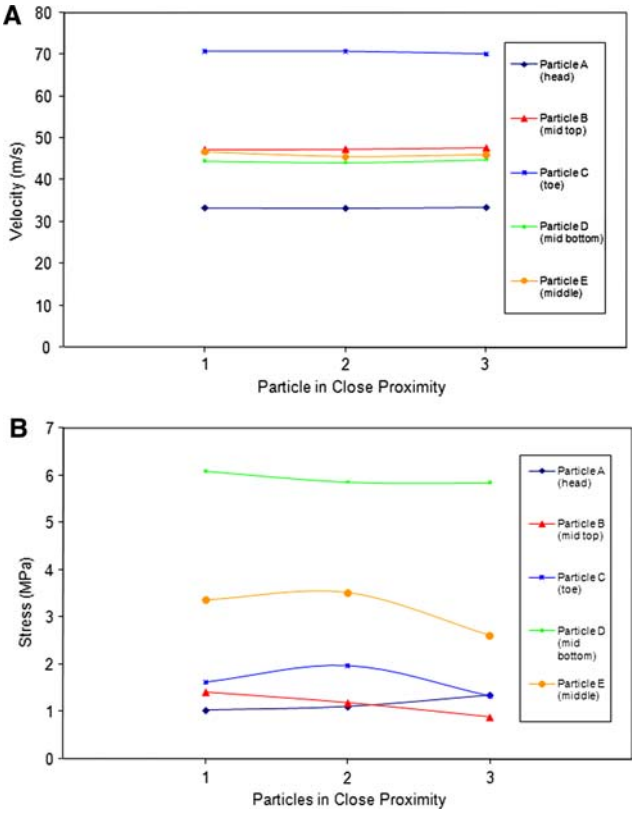


**Fig. 2** Results of variables measured for particles in close proximity to five monitored particles. **a** Maximum *x*-velocity, **b** maximum *xx*-component of stress

Associated horizontal particle velocities initially increase steeply to a maximum then decline at a quickening rate. This observation reflects the increase in the particle velocity as it moves downslope before encountering the horizontal transition whereby it loses much of its kinetic energy and decreases in velocity until deposition. Similar behavior is observed by Campbell et al. [6], Crosta et al. [10] and Staron [40]. Relative maximum horizontal particle velocities shows a similar relationship to that of horizontal particle displacement; the toe of the failure travels the fastest, the head the slowest, and the medial section at a generally steady rate. This observation represents the general extension and spreading of the avalanche body.

It is difficult to recognize any clear trends in the plots of stress versus emplacement time; stresses in each sense (*xx*, *xy*, *yy*) are highly variable, as observed by Campbell et al. ([6]; Fig. 3). Stresses are measured for particles only and not the surrounding force chains, which carry the majority of the stresses present. Consequently, the exact value of stresses is generally unimportant although the relative values remain significant. Stresses typically reach their highest absolute values and experience the highest fluctuations in the early stages of avalanche emplacement, immediately following failure initiation as the avalanche body changes from its pre-failure, in situ state to a flowing mass of material. Stress values and fluctuations remain at high levels as the avalanche approaches the transition to the horizontal runout surface and decrease as the avalanche organizes itself into a steady flow across the horizontal runout surface. This observation is significant as rapidly varying, high stresses may facilitate rock mass fragmentation and disaggregation in real-world rock and debris avalanches. Rarefaction processes, where fragmentation develops from the tensional forces created from the relief of brief but intense collisions, are likely to occur at this time [20, 34]. When considering large-scale volcanic debris avalanches, a number of previous authors have indeed suggested that these early stages of emplacement are most efficient in rock mass break-up with relatively minor fragmentation occurring during transport [3, 34, 41, 43, 49]. Such fragmentation processes may also represent the evolution from block sliding to more dynamic flow conditions as suggested by Voight et al. [49]. In fact, these authors speculate global strength loss of the failed mass is of the order of 75% during this initial emplacement stage. The implication of an evolution from early internal chaos to organized steady flow has also implications as to the formation of commonly observed deposit features. For example, block-scale jigsaw fracture patterns may possibly form during block–block or block–ground impacts and rarefaction effects at early stages of emplacement and be preserved during steady, organized transport in the latter stages.

Particles located in the lower (D) and interior (E) of the avalanche experience greater stress fluctuations than do those particles locate on the free surface (A–C, Fig. 4). In this case, stresses at the bottom and interior of the avalanche are 80–85% and 70–80% higher, respectively, than those on the free surface. A rock mass subject to such stress fluctuations will be more readily fractured and therefore both the early emplacement stages (time-dependent) and lower sections (location-dependent) of the avalanche represent situations where fracture and disaggregation are most likely to occur.

Internal stresses were also evaluated with $PFC^{2D}$'s *measure* tool, which can be used to investigate the change in a range of variables within user-defined circles over a given period of time. Five locations were chosen to observe

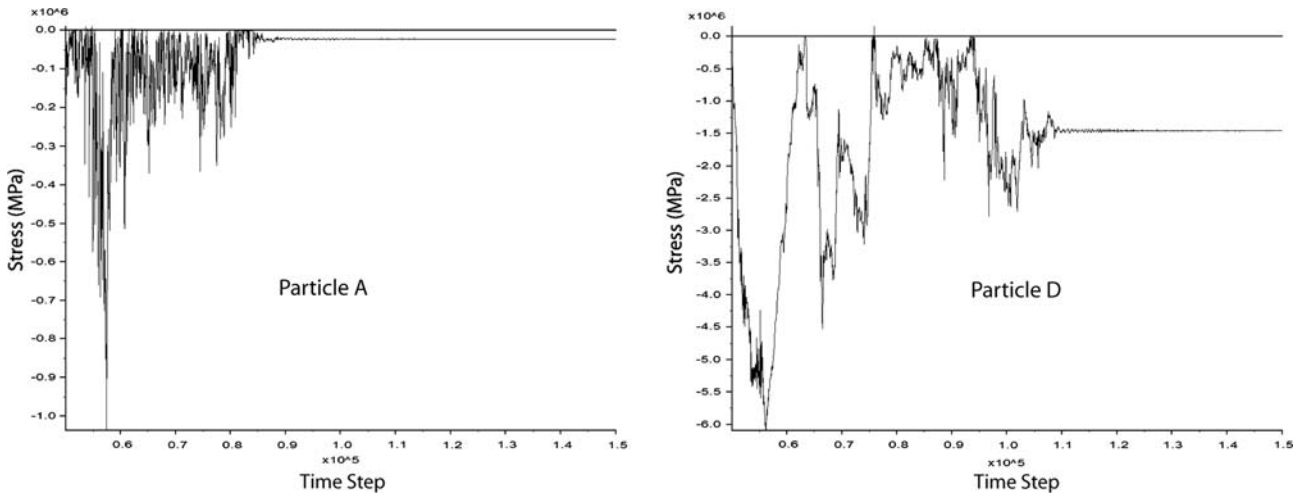


**Fig. 3** Stress (*xx*-component) with time during emplacement for particles A and D. Stresses for each particle monitored and in each sense (*xx*, *xy*, *yy*) behave in a similar fashion. Plot generated by $PFC^{2D}$

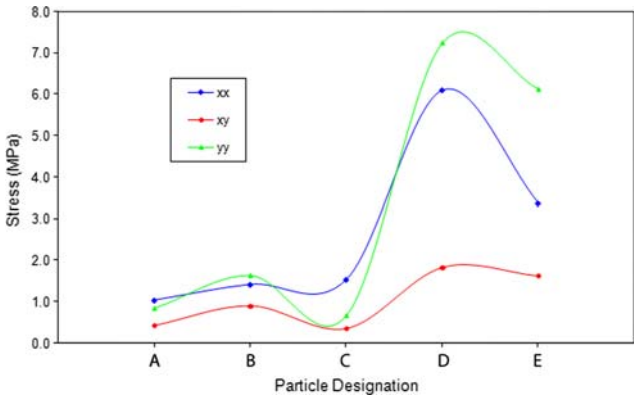


**Fig. 4** Relative maximum stresses experienced by particles located in various parts of the avalanche during emplacement

vertical and horizontal property changes within the avalanche (Fig. 5). The positions of each circle remained constant as the avalanche passes through during failure simulation. Several variables measured using this approach, which are presented in Table 3. The results of this exercise are given in Fig. 6.

Figure 6a and b shows that maximum stresses within the avalanche decrease with increasing vertical ($y$) height and horizontal ($x$) distance. Unlike the particle stresses discussed above, the stresses measured using the circle technique average all stresses within the circle, both particle and force chain. Therefore, this technique provides a much better estimate of continuum average stress where the values are significant. Maximum vertical stresses in this instance are 36.7% higher in the lower third of the failure than the upper third, while maximum horizontal stress is 28.3% higher. Vertical stress decreases by 66.8% from the proximal to distal portion of the avalanche, a function of a decrease in overburden, while horizontal stress decreases by 58.4%.

When these results are considered with the stress measurements discussed above, implications for real-world avalanche behavior can be discussed. In addition to higher stresses in the lower sections of the avalanche, they are also seen to be higher in the avalanches' proximal sections as it piles up at the horizontal transition, which may lead to increased crushing and fragmentation of the lower sections of the avalanche mass in real-world scenarios. Where high initial and rapidly fluctuating stresses may work to disaggregate the avalanche body on the whole, latter development of these spatially dependent stresses increases may promote the development of fragmented or fine-grained basal shearing layers. A similar crushing mechanism due to large basal stresses has also been suggested by Strom (2006), who also suggests that the relative fluidity of this crushed basal layer may lead to upper surface tension and the subsequent development of hummock-type structures common in large-scale rock and debris avalanche deposits. The deforming basal layer may accommodate much of the deformation taking place in the avalanche body during emplacement, allowing the material above to travel relatively undisturbed, and consequently allowing features such as stratigraphic relationships and jigsaw fractured blocks to be preserved upon deposition. Additionally, the basal shearing layer may facilitate increased mobility and long runout and is consistent with laminar plug flow hypotheses [3, 14–16, 34, 37].

In this DEM model, however, individual particles are rigid and cannot fragment. Therefore, a fragmented or fine-grained basal shearing layer cannot develop. As a result, the strain produced in this lower region, which one would expect to be the highest in the avalanche, cannot be relieved and is therefore transferred upward within the failure body. This action is shown in Fig. 6c where strain rate measurements evaluated with the measurement circle technique indicate higher strain rates within the interior of the deposit and lower values toward the upper free surface and the lower ground surface. High strain cannot develop on the free surface of the avalanche and is therefore confined to the interior of the avalanche. Strain rate results are a measure of the instantaneous velocity field and therefore what is measured is the maximum strain rate occurring in each respective section of the avalanche throughout emplacement on the horizontal section of the runout

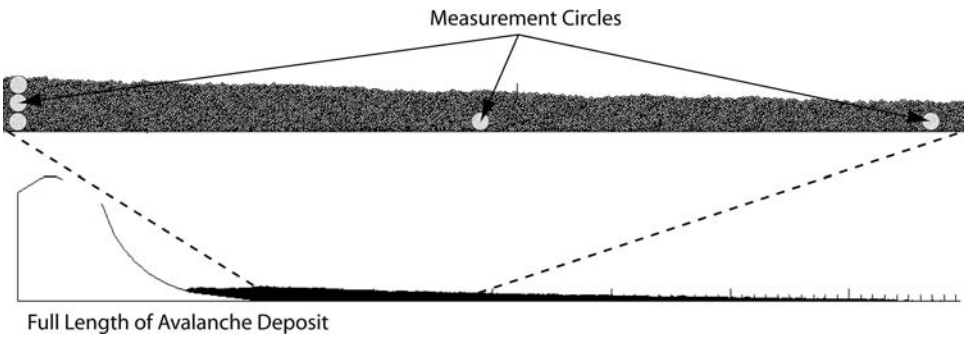


**Fig. 5** Location of measurement circles (35 m in diameter) used to measure the spatial variation of assembly properties

**Table 3** Variables considered with PFC *measure* tool

| Variable | Description |
|---|---|
| Maximum stress | Maximum stresses averaged over the measurement circle (MPa) |
| Maximum strain rate | Strain rate tensors determined through least-squares method [22] |
| Porosity | Ratio of total void area within measurement circle to measurement circle area |
| Coordination number | Mean number of contacts per particle, averages over the measurement circle |
| Sliding fraction | Percentage of contacts which are slipping within the measurement circle |

surface. It is not a cumulative measure of left-over strain. Strain rate decreases linearly with horizontal distance (Fig. 6d). These results may suggest that rock block and stratigraphic deformation is more likely in the interior, proximal section of the particular avalanche.

While strain rate observations may initially appear to reveal a limitation in the modeling technique in that a basal deformation layer cannot develop as it might in natural scenarios, it also highlights the importance of material properties on emplacement characteristics. In an avalanche composed of either weak or widely varying material properties a basal shearing layer may be more likely to develop. In an avalanche comprised either more robust and competent or homogeneous materials such as the rigid particles modeled in $PFC^{2D}$, however, basal shearing layers may be less likely to develop and shear and deformation may be more evenly distributed throughout the avalanche body. A similar suggestion has been discussed by Davies and McSaveney [15] who describe basally weak versus basally strong failures where a lower shearing layer may be more or less likely, respectively, to develop during emplacement. These authors refer to field observations where rock fragmentation has been observed both throughout the full depth of the resultant deposit (basally strong) or confined to basal section (basally weak).

Both porosity (Fig. 6e, f) and coordination number (Fig. 6g, h) indicate a tighter packing at the lower, proximal section of the avalanche; a function of the increased stresses in this area. The mean values of these properties in the pre-failure slope assembly are 0.17 (range 0.14–0.19) and 3.7, respectively. Sliding fraction results (Fig. 6i, j) reveal increased instability in lower proximal section of the avalanche as an increased number of contacts are slipping in this area, also a function of increasing stress with depth.

## 4 Energy analysis

Certain aspects of the avalanches' energy regime can be evaluated by $PFC^{2D}$ (Table 4). As opposed to the previous exercises, simulations were conducted while varying both wall and particle friction ($\mu_w$ and $\mu_p$). The following observations are summarized in Table 5. Gravitational work done on the assembly increase rapidly as the failure moves downslope from its in situ position and gradually decreases as the failure moves onto the horizontal runout surface. Therefore, gravity decreasingly contributes energy to the simulation system and momentum has increased; a transition from potential to kinetic energy. This may be intuitive, but is significant as it shows that gravity by itself can contribute all the initial energies needed to develop high, fluctuating stresses in the first stages of avalanche development. In volcanic flank failure situations, which may often complicated by complex tectonic, magmatic and/or phreatic influences, it is important to show that these forces are not necessarily needed to develop high avalanche mobility or characteristic deposit features. Decreases in the influence of gravity observed with increasing $\mu_p$ and $\mu_w$ suggest that gravity does not complete a full breakdown of the avalanche body as particles are held together by increased frictional strength. As gravitational work decreases, kinetic energy increases accordingly to a sharp maximum, representing the movement of the main mass of the avalanche body down the failure slope and meeting the horizontal transition. Kinetic energy decreases gradually thereafter as the avalanche loses momentum and deposits in the runout area. This behavior reflects that of horizontal particle velocity discussed in Sect. 3. The relative proportions of translational and rotational kinetic energy are 72 and 28%, respectively, revealing that particle motion is mostly translational. The maximum kinetic energy attained by the system decreases with increasing $\mu_p$ and $\mu_w$, again suggesting energy is locked up as potential energy (less avalanche 'flow'). This suggestion is substantiated by a decreasing mean horizontal velocity with increasing $\mu_w$, from 60 m/s at $\mu_w = 0.05$–27 m/s at $\mu_w = 0.3$. Similar kinetic energy relationships are shown by Crosta et al. [10].

Energy dissipated by friction rises steeply to a maximum and gradually decreases with time, signifying the amount of energy dissipated decreases as it is continually being expended. As the initial amount of energy in the system is always the same, the fact that the amount of energy dissipated decreases with increasing $\mu_p$ and $\mu_w$ suggests that there is further energy left in the avalanche system (as potential energy) that has not been expended through emplacement. Essentially, particles are locked together by stronger frictional coupling. Decreased avalanche runout with increasing basal wall friction ($\mu_w$) supports this idea (Sect. 2). These observations are

noteworthy as they stress the importance of material properties in determining avalanche emplacement characteristics. For instance, more competent, high friction materials may tend to be deposited in more proximal locations where lower friction materials would travel further, giving the perception of increased mobility. Such a scenario was modeled by Ward and Day [50] in their reconstruction of the emplacement of the 1980 Mount St. Helens debris avalanche. Energy is dissipated at a faster rate as $\mu_w$ is increased; at $\mu_w = 0.1$ the mean energy dissipated is higher than that at $\mu_w = 0.05$. However, at $\mu_w = 0.2$–$0.3$ the amount of energy dissipated through friction decreases, most likely signifying the onset of particle rolling as a significant process.

The variation in total strain energy stored at all contacts in the assembly during emplacement was also monitored. Strain starts at a maximum and decreases regularly in a sinusoidal manner which decreases in intensity with time. Although it is not particularly clear what mechanisms the sinusoidal behavior may relate to in a real-world rock or debris avalanche, a 'stick-slip' type of movement is envisioned. Strain is highest as the avalanche descends from its in situ position to be temporarily relieved when frictional bonds along the basal failure surface are continually overcome. This behavior continues as frictional coupling between the basal surface and the particles it is in contact with increases after a finite increment of avalanche motion. The mechanism is thus very similar to fault zone stick-slip dynamics. This form of motion in large-scale debris avalanches in difficult to comprehend as they are typically regarded to travel at high velocities (upward of 70–100 m/s) with a certain degree of fluid mobility. Nonetheless, a 'pulsing' or 'caterpillar' motion of this type has been suggested by previous authors [10, 25, 35, 39, 48, 49] although it is unclear how relatable the observation made here may be. Additionally, overcoming high friction in this manner may be the source of friction-generated pseudotachylytes such as those observed by Legros et al. [25] at Peru's Arequipa volcanic debris avalanche deposit. The dependency of the sinusoidal behavior on particle stiffness variation, of which strain energy is a function of, was not explored in detail in this study although it provides an interesting topic for future research [22].

Total assembly strain decreases with increasing $\mu_p$, perhaps, again indicating increased particle rolling in the system. Maximum strain increases with increasing $\mu_w$, however, as strain is built up to higher levels within the avalanche body as the particles in contact with ground surface are bound by stronger contacts. This observation again suggests that at higher values of material and boundary friction, initial potential energy does not have the opportunity to develop fully into kinetic energy.

## 5 Deformation analysis

Further analysis of avalanche emplacement was performed by introducing colored markers into each of the simulations detailed above. Both vertical stripes and a configuration generally representative of stratigraphic layers were used to obtain a qualitative understanding of the deformation during emplacement (Fig. 7). Simulations were run in which each vertical stripe or stratigraphic layer possessed the same material properties as its neighbors and in which the properties varied between layers. As performed for the energy analysis, changes in deformation were observed for various values of $\mu_p$ and $\mu_w$. Ranges of $\mu_w$ values from 0.05 to 0.3 and $\mu_p$ values of 0.25–3.0 were considered. The general deposit shape in all case was similar to that produced by Crosta et al. [10] and Campbell et al. [6] for their large volume failures where the center of mass of the deposit is located more proximally than distally.

### 5.1 Uniform material properties

Deformation of the avalanche body during emplacement was first analyzed by using vertical stripes. At $\mu_w = 0.05$ (low wall friction), the lower region of proximal section of the avalanche moves more rapidly than the upper section down the failure slope (Fig. 8). At a point in the medial section of the failure, the upper and lower sections travel together at the same rate. In the distal sections, the upper region of the failure near the free surface overtakes the lower region. This collective motion works to stretch and thin the failure and represents a changing vertical velocity gradient from proximal to distal sections of the avalanche. Increases in $\mu_p$ show the same general characteristics though deformation of the individual stripes appears to increase through compression of the medial section of the avalanche body as the failure slows upon reaching the horizontal transition. An up-welling of the medial particles is subsequently observed and retained after moment cessation (Fig. 9a). Deformation of the interior of the avalanche body in this manner, rather than basal layer deformation as might occur in a real-world scenario, is consistent with increased interior strain rate results discussed in Sect. 3. Similar observations are made when $\mu_w$ is increased to 0.1, although to a lesser degree as the avalanche is not stretched as thinly. At higher levels of $\mu_p$, the compression and up-welling of the medial avalanche section is again observed just distally from the thickest segment of the deposit (Fig. 9b). Deformation in the proximal section of the slide is reduced at $\mu_w = 0.2$ as stretching of the avalanche body is less pronounced; deformation in the distal section increases, observed as particles in the upper regions cascading off the granular pile. The level at which particles cascade down the free

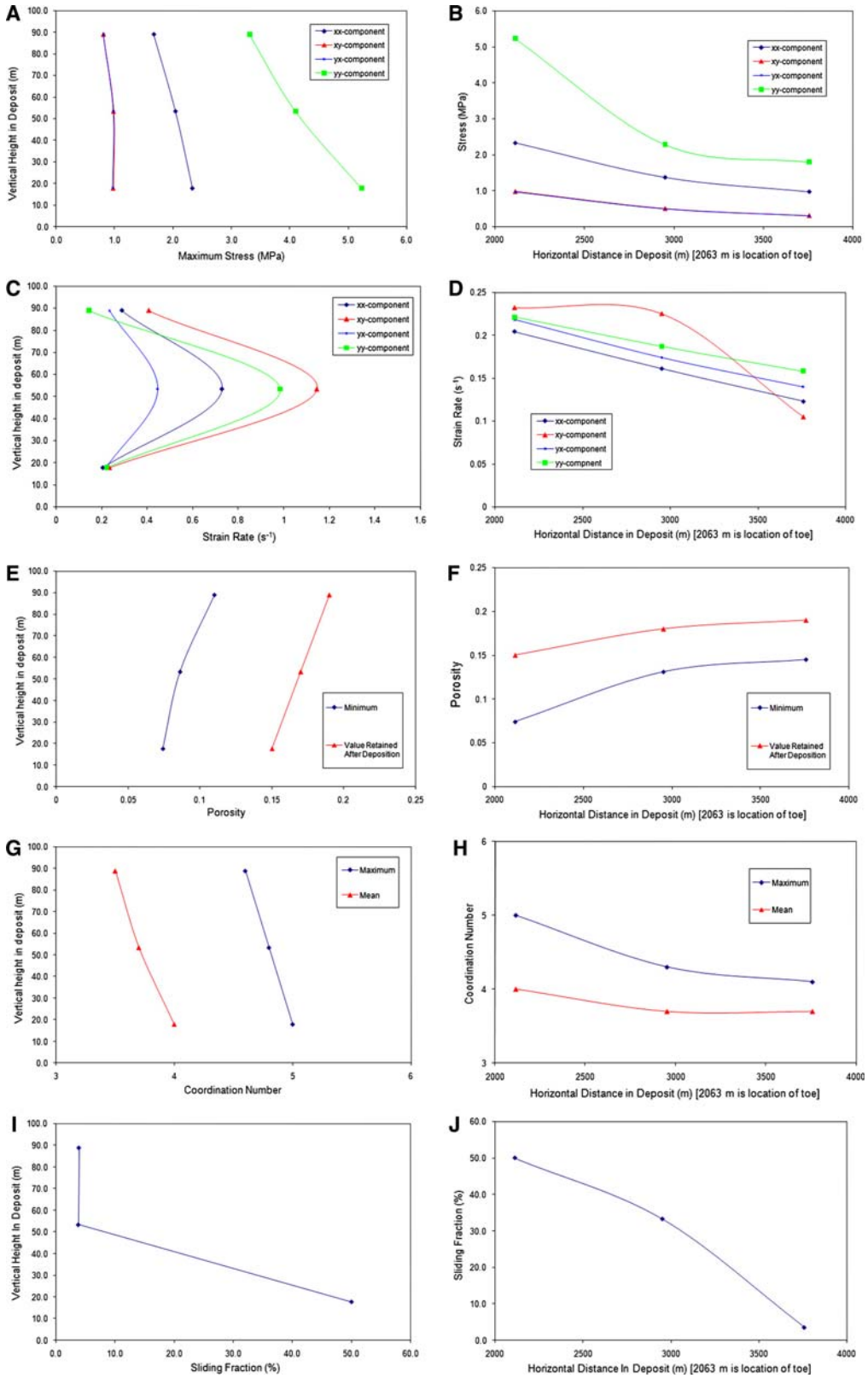


**Fig. 6** Graphical results of the measurement circle spatial property analysis. **a** Maximum stress versus vertical position, **b** maximum stress versus horizontal position, **c** maximum strain rate versus vertical position, **d** maximum strain rate versus horizontal position, **e** porosity versus vertical position, **f** porosity versus horizontal position, **g** coordination number versus vertical position, **h** coordination number versus horizontal position, **i** maximum sliding fraction versus vertical position, **j** maximum sliding fraction versus horizontal position

**Table 4** Assemblage energy variables monitored; energy tracing begins at the instance of failure and ends at motion cessation

| Energy variable | Description |
|---|---|
| Body | Total accumulated work done by all body forces on the assembly. Gravity is the only body force in this experiment |
| Frictional | Total energy dissipated by frictional sliding at all contacts in the assembly |
| Kinetic | Total kinetic energy of all particles in the assembly (translational and rotational motion) |
| Strain | Total strain energy of the entire assembly stored at all contacts |

**Table 5** Summary of the energy variable behavior with variation in $\mu_p$ and $\mu_w$

| Energy variable | Behavior with increasing $\mu_p$ | Behavior with increasing $\mu_w$ |
|---|---|---|
| Body | Decreases | Decreases |
| Frictional | Decreases | Decreases |
| Kinetic | Decreases | Decreases |
| Strain | Decreases | Increases |

surface rises vertically within the avalanche as $\mu_p$ increases. Similar behavior is observed as $\mu_w$ is increased to 0.3 although mean particle displacement and failure deformation are further reduced as the failure mass is increasingly bound to the failure surface through greater frictional coupling (Fig. 10). In summary, increases in $\mu_w$ decrease the mean horizontal displacement of the failure mass while increases in $\mu_p$ decrease the depth at which particles cascade off the upper surface of the pile.

When the stratigraphic layer geometry is considered, little deformation of the individual layers was observed at lower values of $\mu_w$. Each layer is stretched thinly in the medial section of the deposit and thickens toward the proximal and distal edges. Little change in layer deformation is observed with increasing $\mu_p$. Similar deformation observations are made as $\mu_w$ is increased to 0.1 although layer deformation generally increases. Stratigraphic layers undulate to a higher degree and the medial compressional up-welling feature is at its largest. Again, as $\mu_w$ is increased to 0.2, little change in deformation is observed. At the highest value of $\mu_w$ (0.3), the stratigraphic layers begin to fold over themselves as the lowest distal particles are bound to the failure surface, a phenomenon that increases with increasing $\mu_p$ as frictional coupling effects become stronger. Similar layer deformation was observed by Campbell et al. [6]. Original stratigraphic relationships were retained in each case.

## 5.2 Variable material properties

Here, the material properties of the simulated volcanic stratigraphic layers were alternated such as would be found in real-world systems. Variations of $\mu_p$ and particle mass density were considered individually as was the alteration of weak (low friction/low density), medium (medium friction/medium density), and strong (high friction/high density) layers.

Increases in particle mass density lead to more structure being created in the internal layers within the deposit (Fig. 11). This takes the form of a medial compressional up-welling structure with a series of similar structures of smaller-scale located distally. Visually, this feature is remarkably similar to cross-section sketches presented by Endo et al. [19] in their description of hummock features at the debris avalanche deposit at Ontake volcano, central Japan, and along with the internal stratigraphies qualitatively appear to deform the avalanche body in a right-lateral sense. Topography is gently undulating, reflecting and conformable with the layered stratigraphy below.

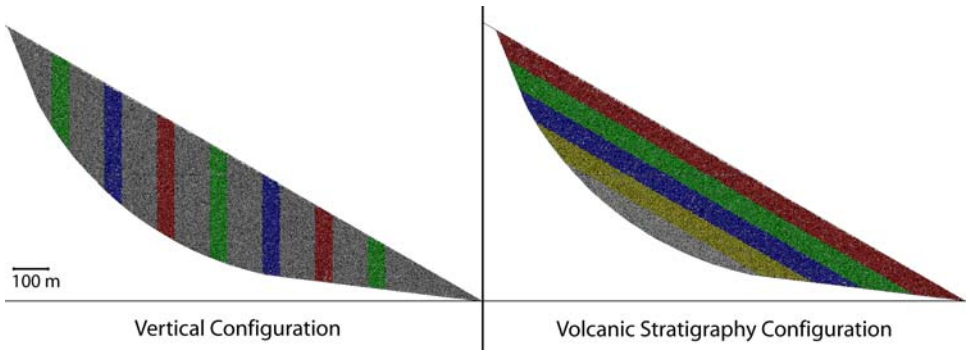


**Fig. 7** Marker patterns used for deformation analysis

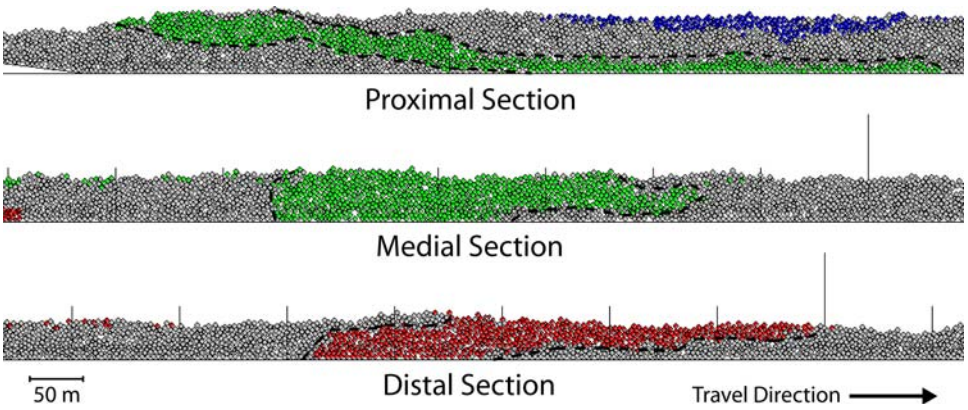


**Fig. 8** Avalanche deposit at $\mu_w = 0.05$ and $\mu_p = 0.75$ showing differing spatial deformation

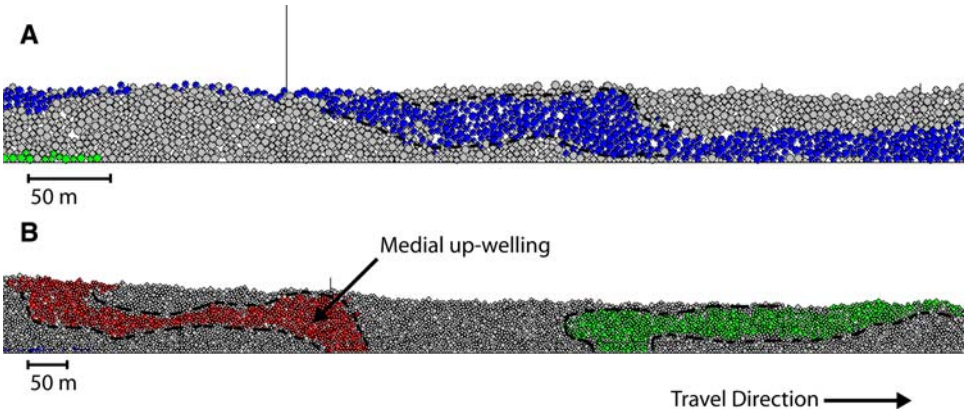


**Fig. 9** **a** Compressional up-welling internal deformation structure ($\mu_w = 0.05$, $\mu_p = 0.5$). **b** Up-welling of particles in medial section of the deposit. Note the mode of deformation switching from left- to right-lateral just beyond this structure ($\mu_w = 0.1$, $\mu_p = 1.0$). Note separate scales for **a** and **b**

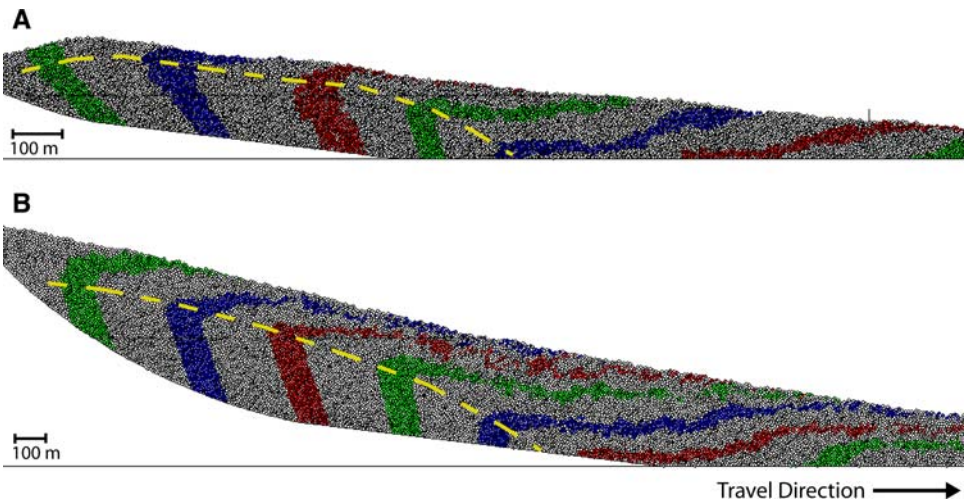


**Fig. 10** **a** Avalanche deformation at $\mu_w = 0.2$. *Dashed lines* indicate denote vertical point where particles cascade distally from the granular pile. **b** Avalanche deformation at $\mu_w = 0.3$. Note separate scales for **a** and **b**; $\mu_p = 0.75$ in each case

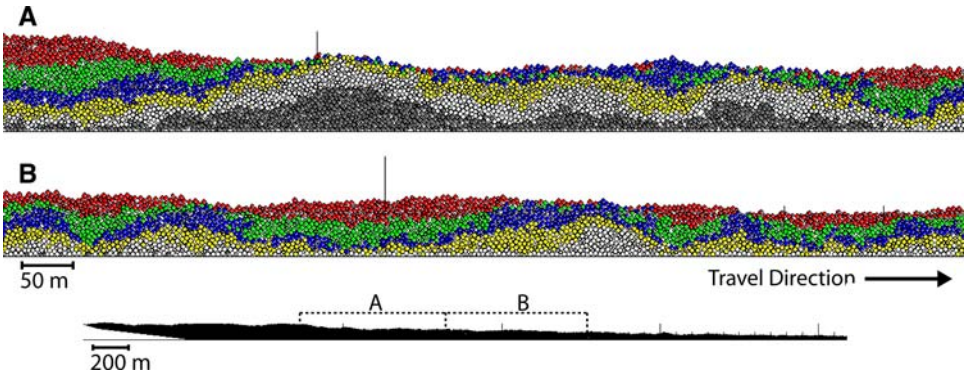


**Fig. 11** Topography and close-ups of simulations with the largest material property differences (weak vs. strong layers). The medial up-welling structure is visible in the upper close-up (**a**). Note the separate scale for zoom. Note the addition of an additional stratigraphic layer (*dark grey*) as compared to Fig. 7

Stratigraphy is generally preserved except for in the upper regions of the distal sections of the failure. Increasing $\mu_p$ stems further develops the medial up-welling feature and internal layer deformation, particularly in more distal sections. The upper stratigraphic layers have been stretched, so thinly they are completely separated. Topography is generally subdued and featureless; typically mirroring stratigraphic undulations below although some layer deformation is present in the distal sections of the deposit.

When the weak ($\mu_p = 0.25$, density $= 500$ kg/m$^3$) versus medium ($\mu_p = 0.75$, density $= 2{,}000$ kg/m$^3$) layer stratigraphies are analyzed, internal stratigraphic deformation is observed, which is generally reflected in the topography. This deformation increases as the medium versus strong ($\mu_p = 3.0$, density $= 3{,}500$ kg/m$^3$) layer configuration is introduced and takes the form of highly undulating layers proximally, large medial up-welling structures and increasing distal stratigraphic deformation. Combining the weak and strongest layers reveals the most significant topographic undulations and internal deformation structures (Fig. 11). Alternating the location of the weakest and strongest layers, where the weakest layer is in full contact with the failure surface, leads to a qualitative increase in stratigraphic deformation and associated topographic extremes. However, common to all simulations is a series of compressional upwelling structures decreasing in scale distally.

The travel characteristics (runout, deposit length, and thickness) of the above stratigraphic simulations were also monitored. No clear trends were recognized when alternating the properties of each layer although runout distances remained generally consistent. It is observed, however, that the longest avalanche runouts occur in the simulations with the largest material property differences (weak vs. strong system). Runout generally decreases with increasing $\mu_p$ and particle mass density. Again, original stratigraphic relationships were generally retained upon deposition.

## 6 Conclusions

The above modeling has provided useful insight concerning the emplacement mechanics of an unbonded granular system in relation to large-scale rock and debris avalanches. This scenario is generally representative of volcanic flank or sector collapses. The effects of frictional properties on deposit morphology are evident; boundary friction ($\mu_w$) affects the system to a larger degree than does constituent particulate friction ($\mu_p$). Mechanical analysis of the avalanche system has shown that the initial stages of failure are chaotic in terms of stresses and strains occurring within the failure; a likely period of increased block fragmentation. Velocity, and therefore kinetic energy, is highest as the avalanche approaches the transition to the horizontal runout surface, whereby the failure settles into a generally steady and organized flow as velocity steadily decreases until deposition. The transition to horizontal motion therefore represents a key moment during emplacement as stress fields must readjust to accommodate this change, promoting block/rock mass fragmentation. On the basis of observations made during field studies of large-scale volcanic debris avalanche deposits, several authors have also concluded that the changing stress regime associated with this transition is influential in promoting block fragmentation [37]. Energy measurements have verified several intuitive assumptions and confirmed that avalanche deposition is generated by its encounter with the horizontal runout surface.

In addition to early stages of increased and rapidly fluctuating stresses, measurements reveal that stresses are highest in the lower proximal regions of the failure, a region where particle and block fragmentation and deformation may likely occur. The stresses and displacements observed quantify the degree to which the toe and free surface of the failure are relatively unrestricted as compared to lower and interior sections of the avalanche. This

is important for two reasons. First, an unhindered toe, or avalanche front, facilitates stretching and thinning of the avalanche body, allowing it to attain a higher energy and promoting long runout. Second, lack of stress at the top of the failure, or in the latter stages of emplacement in general, may help to preserve angular surface or jigsaw fractured blocks often found in large avalanche deposits, therefore explaining their presence [6].

Experiments have shown that a degree of strain is created in interior the avalanche body due to the contradicting effects of the ground and free surfaces. Accordingly, increased deformation has been recognized in this interior region through layer deformation analysis. These observations may be the result of an inability for the model particles to fragment under high stresses/strains but may also highlight the importance of constituent material properties on avalanche emplacement characteristics. If model particles were able to replicate weak natural materials in terms fragmentation, for instance, a basal shearing layer may develop which would influence both mobility and deposit features. Also, time-dependent global strain observations indicate the large-scale granular failure may perhaps travel in a pulsing motion as friction is locally and continually overcome.

Original stratigraphic relationships are retained upon deposition although individual layers have been drastically thinned and stretched, the top layers more so than those on the bottom. This phenomenon was also observed in DEM experiments of Campbell et al. [6] and is significant as the retention of original stratigraphic relationships is often observed in the deposits of large-scale rock and debris avalanches [7, 35, 37, 38]. Thus, the collective motion of the DEM simulation illustrates how large-scale avalanches may spread out in an organized fashion from the base of the failure source, as suggested for real-world events. Macroscopic deformation of the avalanche body shifts from left- to right-lateral at a point in the proximal to medial section of the failure where the deposit is thickest. Proximally from this point the granular material appears to 'fall back' on itself while distally the material cascades off the pile, extending the avalanche in a right-lateral sense. This change in behavior develops from the avalanches encounter with the transition to the horizontal runout surface.

Several limitations with this modeling approach deserve attention. Intuitively, the coarse and two-dimensional nature of the DEM does not create an ideal debris avalanche system. For instance, the effects of lateral spreading and associated margin structures cannot be examined as it involves the out-of-screen dimension. It is assumed in such a model, however, that the lack of third dimension movement does not considerably affect the flow dynamics in the principal flow direction [40]. Also, the influence of fine-grained or saturated sediments and dynamic flow conditions often suggested for large-scale avalanche emplacement is thus far difficult to consider. Furthermore, as these models have been conducted with completely unbonded granular material, they are limited in their capacity to develop characteristic debris avalanche topography such as hummocks, steep margins, etc. The topography created by the unbonded simulations consists only of broad undulations at its most extreme. The unbonded simulations lack the ability to consider realistic situations such as particle and block fragmentation and effects these processes have on emplacement and deposit features. These processes are considered a fundamental aspect of large-scale avalanche emplacement and the mechanics behind it should be considered in detail but are beyond the scope of this current study [43]. Lastly, as the runout area is a simple horizontal surface, the influence of varying topography has not been considered. This was done in part for consistency with previous studies but provides a promising topic for future study. The observation discussed herein should therefore be regarded as first-order approximations of real-world events.

These limitations, however, rather than being detrimental to the results, provide a wealth of topics for future study. For instance, the changes in deposit features observed when particle bonding is introduced, creating a more competent initial material, may be dramatic. Such a technique will be valuable in investigating the influence of initial material strengths on emplacement mechanics. Furthermore, a bonded particle approach may allow block sliding effects to be more realistically considered as this motion is often restricted by particle rolling in the simulations discussed above. The unbonded avalanche simulation results presented here, however, establish a valuable foundation for studies of this nature.

**Acknowledgements** N. Thompson would like to thank Bournemouth University which provided the studentship that has funded this research. The authors would also like to thank David Potyondy, Peter Cundall, and Roger Hart of HCItasca for their reviews and encouraging comments as well as Alexander Preh and an anonymous reviewer, whose suggestions have helped to improve the manuscript.

## References

1. Azzoni A, de Freitas MH (1995) Experimentally gained parameters, decisive for rock fall analysis. Rock Mech Rock Eng 28:111–124. doi:10.1007/BF01020064
2. Barla G, Barla M (2001) Investigation and the modelling of the Brevna Glacier rock avalanche on the Mont Blanc range. Eurorock 2001:35–40
3. Belousov A, Belousova M, Voight B (1999) Multiple edifice failures, debris avalanches and associated eruptions in the Holocene history of Shiveluch volcano, Kamchatka, Russia. Bull Volcanol 61:324–342. doi:10.1007/s004450050300
4. Campbell CS (1989) Self-lubrication for long runout landslides. J Geol 97:653–665

5. Campbell CS (1990) Rapid granular flows. Annu Rev Fluid Mech 22:57–92. doi:10.1146/annurev.fl.22.010190.000421
6. Campbell CS, Cleary PW, Hopkins M (1995) Large-scale landslide simulations: global deformation, velocities and basal friction. J Geophys Res 100:8267–8273. doi:10.1029/94JB00937
7. Clavero JE, Sparks RSJ, Huppert HA (2002) Geological constraints on the emplacement mechanism of the Parinacota debris avalanche, northern Chile. Bull Volcanol 64:40–54. doi:10.1007/s00445-001-0183-0
8. Cleary PW, Campbell CS (1993) Self-lubrication for long runout landslides: examination by computer simulation. J Geophys Res 98:21911–21924. doi:10.1029/93JB02380
9. Cleary PW, Mériaux C, Owen PJ (2007) Prediction of quasi-static fall of planar granular columns using 2D discrete element modeling. In: Proceedings of the fourth international conference on discrete element methods, 27–29 August, Brisbane, Australia, CD-ROM, 12 pp
10. Crosta G, Calvetti F, Imposimato S, Roddeman D, Frattini P, Agliardi F (2001) Granular flows and numerical modelling of landslides (online). Universita di Milano, available from: http://damocles.irpi.pg.cnr.it/docs/reports/Granular_Flows_Thematic_Report.pdf. Accessed 30 Nov 2006
11. Cundall PA (1971) A computer model for simulating progressive large scale movements in blocky rock systems. In: Proceedings of the symposium of the international society of rock mechanics, Nancy, France, 1, paper no. II-8
12. Cundall PA, Strack ODL (1979) A discrete numerical model for granular assemblies. Geotechnique 29:47–65
13. Davies TRH, McSaveney MJ (1999) Runout of dry granular avalanches. Can Geotech J 36(2):313–320. doi:10.1139/cgj-36-2-313
14. Davies TRH, McSaveney MJ (2002) Dynamic simulation of the motion of fragmenting rock avalanches. Can Geotech J 36:313–320. doi:10.1139/cgj-36-2-313
15. Davies TRH, McSaveney MJ (2008) The role of rock fragmentation in the motion of large landslides. Eng Geol doi:1016/j.enggeo.2008.11.004
16. Davies TRH, McSaveney MJ, Beetham RD (2006) Rapid block glides: slide-surface fragmentation in New Zealand's Waikaremoana landslide. Q J Eng Geol Hydrogeol 39:115–129. doi:10.1144/1470-9236/05-041
17. Deluzarche RB, Dedecker F, Fry JJ (2003) Static and dynamic analysis of stability of rocky slopes via particle methods. In: Konietzky H (ed) Numerical modelling in micromechanics via particle methods (Proceedings of the 1st international PFC symposium, Gelsenkirchen, Germany, 6–8 November 2002), Balkema, Lisse, pp 125–131
18. Drake TG (1990) Structural features in granular flows. J Geophys Res 95:8681–8696. doi:10.1029/JB095iB06p08681
19. Endo K, Sumita M, Machida M, Furuichi M (1989) The 1984 collapse and debris avalanche deposits of Ontake volcano, central Japan. In: Latter JH (ed) Volcanic Hazards: IAVCEI proceedings in volcanology 1. Springer, Berlin, Heidelberg, pp 210–229
20. Glicken HX (1991) Sedimentary architecture for large volcanic debris avalanches. In: Smith GA, Fisher RV (eds) Sedimentation in volcanic settings. SEPM Special Publications, 45, pp 99–106
21. Glicken HX (1998) Rock slide debris avalanche of May 18, 1980 Mount St. Helens volcano, Washington. Bull Geol Soc Jpn 49:55–105
22. Itasca (2004) Theory and background. Third edition (version 3.1), November, 2004
23. Le Friant A, Boudon G, Komorowski JC, Heinrich P, Semet MP (2006) Potential flank-collapse of Soufriére volcano, Guadeloupe, Lesser Antilles? Numerical simulation and hazards. Nat Hazards 39:381–393. doi:10.1007/s11069-005-6128-8
24. Legros F (2002) The mobility of long runout landslides. Eng Geol 63:301–331. doi:10.1016/S0013-7952(01)00090-4
25. Legros F, Cantagrel JM, Devourd B (2000) Pseudotachylyte (Frictionite) at the base of the Arequipa Volcanc Landslide deposit (Peru): implications for emplacement mechanisms. J Geol 108:601–611. doi:10.1086/314421
26. Lorig LJ, Gibson W, Alvial J, Cuevas J (1995) Gravity flow simulations with the Particle Flow Code (PFC). ISRM News J 3:18–24
27. Melosh HJ (1979) Acoustic fluidization—a new geologic process? J Geophys Res 84:7513–7520
28. Morgan JK (2006) Volcanotectonic interactions between Mauna Loa and Kilauea: insights from 2-D discrete element simulations. J Volcanol Geotherm Res 151:109–131. doi:10.1016/j.jvolgeores.2005.07.025
29. Morgan JK, McGovern PJ (2003) Discrete element simulations of volcanic spreading: implications for the structure of Olypmus Mons, 35th lunar and planetary science conference, abstract 2008
30. Morgan JK, McGovern PJ (2005) Discrete element simulations of gravitational volcanic deformation. 1: deformation structures and geometries. J Geophys Res 110:B05403. doi:10.1029/2004JB003253
31. Morgan JK, McGovern PJ (2005) Discrete element simulations of gravitational volcanic deformation. 2: mechanical analysis. J Geophys Res 110:B05403. doi:10.1029/2004JB003252
32. Preh A, Poisel R (2006) Models for landslide behaviour with large displacements by the particle Flow Code. Felsbau 25:31–37
33. Reid ME, Christian SB, Brien DL (2000) Gravitational stability of three-dimensional stratovolcano edifices. J Geophys Res 105:6043–6056. doi:10.1029/1999JB900310
34. Reubi O, Hernandez J (2000) Volcanic debris avalanche deposits of the upper Marrone valley (Cantal Volcano, France): evidence for contrasted formation and transport mechanisms. J Volcanol Geotherm Res 102:271–286. doi:10.1016/S0377-0273(00)00191-8
35. Schneider JL, Fisher RV (1998) Transport and emplacement mechanisms of large volcanic debris avalanches: evidence from the northwest sector of Cantal volcano (France). J Volcanol Geotherm Res 83:141–165. doi:10.1016/S0377-0273(98)00016-X
36. Schuster RL, Crandell DR (1984) Catastrophic debris avalanches from volcanoes. IV international symposium on landslides proceedings, vol 1, pp 567–572
37. Shea T, de Vries B, Pilato M (2008) Emplacement mechanisms of contrasting debris avalanches at Volcán Mombacho (Nicaragua), provided by structural and facies analysis. Bull Volcanol 70:899–921. doi:10.1007/s00445-007-0177-7
38. Siebert L (1984) Large volcanic debris avalanches: characteristics of source areas, deposits and associated eruptions. J Volcanol Geotherm Res 22:163–197. doi:10.1016/0377-0273(84)90002-7
39. Sousa J, Voight B (1995) Multiple-pulsed debris avalanche emplacement at Mount St. Helens in 1980: evidence from numerical continuum flow simulations. J Volcanol Geotherm Res 66:227–250. doi:10.1016/0377-0273(94)00067-Q
40. Staron L (2008) Mobility of long-runout rock flows: a discrete numerical investigation. Geophys J Int 172:455–463. doi:10.1111/j.1365-246X.2007.03631.x
41. Takarada S, Ui T, Yamamoto Y (1999) Depositional features and transportation mechanism of valley-filling Iwasegawa and Kaida debris avalanches, Japan. Bull Volcanol 60:508–522. doi:10.1007/s004450050248
42. Tommasi P et al. (2003) Analysis of rock avalanches generated by large planar rock slides by means of numerical methods for discontinua. Technology roadmap for rock mechanics (Proceedings of the 10th congress of the ISRM, Johannesburg), vol 2, pp 1235–1240

43. Ui T (1983) Volcanic dry avalanche deposits—identification and comparison with nonvolcanic stream deposits. J Volcanol Geotherm Res 18:135–150. doi:10.1016/0377-0273(83)90006-9
44. Uttini A, Apuani T, Massetti M, Vezzoli L, Corazzato C (2006) First contribution to debris slope stability analysis of Sciara del Fuoco (Stromboli island, Italy) via particle numerical modeling. Geophys Res Abstr 8:08103
45. Uttini A, Apuani T, Massetti M (2007) The Sciara del Fuoco debris stability (Stromboli volcano, Italy): a distinct element numerical modelling of possible triggering mechanisms. Geophys Res Abstr 9:04319
46. Voight B (2000) Structural stability of andesite volcanoes and lava domes. Philosophical Transactions of the Royal Science A. Math Phys Eng Sci 358:1663–1703. doi:10.1098/rsta.2000.0609
47. Voight B, Elsworth D (1997) Failure of volcano slopes. Geotechnique 47:1–31
48. Voight B, Glicken H, Janda RJ, Douglass PM (1981) Catastrophic rockslide avalanche of May 18. In: Lipman PW, Mullineaux DR (eds) The 1980 eruption of Mount St. Helens, Washington, U.S. Geological Survey Professional Paper, 1250, pp 347–377
49. Voight B, Janda RJ, Glicken HX, Douglass PM (1983) Nature and mechanics of the Mount St. Helens rockslide-avalanche of 18 May 1980. Geotechnique 33:243–273
50. Ward SN, Day S (2006) Particulate kinematic simulations of debris avalanches: interpretation of deposits and landslide seismic signals of Mount Saint Helens, 1980 May 18. Geophys J Int 167:991–1004. doi:10.1111/j.1365-246X.2006.03118.x